The Astrophysical Journal, 827:25 (13pp), 2016 August 10 doi:10.3847/0004-637X/827/1/25

THE ORBIT OF THE L DWARF + T DWARF SPECTRAL BINARY SDSS J080531.84+481233.0*

Adam J. Burgasser[1], Cullen H. Blake[2], Christopher R. Gelino[3], Johannes Sahlmann[4], and Daniella Bardalez Gagliuffi[1]
[1] Center for Astrophysics and Space Science, University of California San Diego, La Jolla, CA 92093, USA; aburgasser@ucsd.edu
[2] Department of Physics and Astronomy, University of Pennsylvania, Philadelphia, PA 19104, USA
[3] NASA Exoplanet Science Institute, Mail Code 100-22, California Institute of Technology, 770 South Wilson Avenue, Pasadena, CA 91125, USA
[4] European Space Agency, European Space Astronomy Centre, P.O. Box 78, Villanueva de la Caada, E-28691 Madrid, Spain
Received 2016 March 26; revised 2016 May 17; accepted 2016 May 17; published 2016 August 3

ABSTRACT

SDSS J080531.84+481233.0 is a closely separated, very-low-mass (VLM) binary identified through combined-light spectroscopy and confirmed as an astrometric variable. Here we report four years of radial velocity monitoring observations of the system that reveal significant and periodic variability, confirming the binary nature of the source. We infer an orbital period of 2.02 ± 0.03 years, a semimajor axis of $0.76^{+0.05}_{-0.06}$ au, and an eccenticity of 0.46 ± 0.05, consistent with the amplitude of astrometric variability and prior attempts to resolve the system. Folding in constraints based on the spectral types of the components (L4 ± 0.7 and T5.5 ± 1.1), corresponding effective temperatures, and brown dwarf evolutionary models, we further constrain the orbital inclination of this system to be nearly edge-on (90° ± 19°), and deduce a large system mass ratio ($M_2/M_1 = 0.86^{+0.10}_{-0.12}$), substellar components ($M_1 = 0.057^{+0.016}_{-0.014}$ $M_\odot$, $M_2 = 0.048^{+0.008}_{-0.010}$ $M_\odot$), and a relatively old system age (minimum age $= 4.0^{+1.9}_{-1.2}$ Gyr). The measured projected rotational velocity of the primary ($V_{\rm rot} \sin i = 34.1 \pm 0.7$ km s^{-1}) implies that this inactive source is a rapid rotator (period $\lesssim 3$ hr) and a viable system for testing spin–orbit alignment in VLM multiples. Robust model-independent constraints on the component masses may be possible through measurement of the reflex motion of the secondary at wavelengths in which it contributes a greater proportion of the combined luminence, while the system may also be resolvable through sparse-aperature mask interferometry with adaptive optics. The combination of well-determined component atmospheric properties and masses near and/or below the hydrogen minimum mass make SDSS J0805+4812AB an important system for future tests of brown dwarf evolutionary models.

Key words: binaries: spectroscopic – brown dwarfs – stars: individual (SDSS J080531.84+481233.0) – stars: low-mass

1. INTRODUCTION

Multiple systems, particularly short-period binaries, are key targets for fundamental measurements of individual stars. While the orbital periods of these systems allow us to infer their total system mass, the gold standard is the determination of individual component masses through absolute astrometry or reflex motion from both components, and radii through transits or modeling of the spectral energy distribution. These quantities can be used to directly test stellar structure models (Stassun et al. 2006; Torres et al. 2010; Johnson et al. 2011; Borkovits et al. 2013). For brown dwarfs, objects with insufficient mass to sustain core hydrogen fusion (Kumar 1962, 1963; Hayashi & Nakano 1963), such systems provide empirical tests of evolutionary cooling models, where the combination of mass and atmospheric properties, in some cases coupled with external information on system age or composition, can be directly compared to model predictions (Dupuy et al. 2009, 2014; Kasper et al. 2009; Konopacky et al. 2010; Liu et al. 2010; Burgasser et al. 2012). In addition, given that a significant fraction (15%–30%) of very low mass (VLM; $M \leqslant 0.1\,M_\odot$) stars and brown dwarfs are found in $a \lesssim 20$ au binary systems (e.g., Allen 2007; Burgasser et al. 2007; Duchêne & Kraus 2013; Dupuy et al. 2013 and references therein), the orbital properties of these systems and degree of spin–orbit alignment provide necessary constraints on brown dwarf formation mechanisms, which are still under investigation (Bate 2009, 2012; Offner et al. 2010; Kratter 2011; Parker & Meyer 2014).

Detecting resolvable VLM binaries with short enough orbital periods for mass measurement can be challenging, and just over a dozen such systems are currently known (e.g., Dupuy & Liu 2011). Even fewer radial velocity (e.g., Basri & Martín 1999; Reid et al. 2002; Blake et al. 2008; Joergens et al. 2010; Burgasser et al. 2012) and astrometric variables (e.g., Dahn et al. 2008; Dupuy & Liu 2012; Sahlmann et al. 2013) are known, and in many cases the component properties of these systems cannot be resolved. Only a single eclipsing brown dwarf-brown dwarf system has been found, a ~1 Myr old system in Orion (Stassun et al. 2006); although several brown-dwarf-mass objects have been found to transit more massive stars (e.g., Deleuil et al. 2008; Johnson et al. 2011; Schaffenroth et al. 2014), enabling radii measurements that are in many cases inconsistent with models (e.g., Burrows et al. 2011). Fortunately, the spectra of M-, L- and T-type brown dwarfs are sufficiently distinct that binaries composed of these sources can often be discerned and characterized through unresolved spectroscopy; these are the VLM spectral binaries (Cruz et al. 2004; Burgasser et al. 2010; Bardalez Gagliuffi et al. 2014). A dozen of these systems have been identified and confirmed over the past decade, over half of which have compact orbits ($\lesssim$2 au) enabling simultaneous

* Some of the data presented herein were obtained at the W.M. Keck Observatory, which is operated as a scientific partnership among the California Institute of Technology, the University of California and the National Aeronautics and Space Administration. The Observatory was made possible by the generous financial support of the W.M. Keck Foundation.

Table 1
NIRSPEC Observations and Measurements

UT Date	MJD	t_{int} (s)	Airmass	Conditions	S/N	RV[a] (km s^{-1})	$V_{rot} \sin i$[a] (km s^{-1})
2012 Apr 02	56019.28665	2400	1.18	clear, 0.″7	23	14.7 ± 0.3	38.0 ± 0.4
2012 Nov 27	56258.47308	2400	1.30	p. cloudy, 0.″5	16	7.6 ± 0.5	37.2 ± 0.7
2013 Jan 20	56312.46857	3000	1.15	clear, 1″	10	9.3 ± 0.5	36.1 ± 0.8
2013 Feb 05	56328.48671	3000	1.33	clear, 1″	12	7.7 ± 0.5	37.0 ± 1.2
2013 Sep 17	56552.62423	2400	1.78	clear, 1″–2″	12	7.6 ± 0.8	37.3 ± 1.8
2013 Oct 16	56581.62182	2500	1.28	p. cloudy, 0.″8	19	10.8 ± 0.3	37.2 ± 0.5
2014 Apr 13	56760.26506	3000	1.15	clear, 0.″5	21	14.4 ± 0.4	35.9 ± 0.9
2014 Dec 08	56999.59552	3000	1.14	clear, 0.″8	7	6.9 ± 1.5	26.7 ± 0.9[b]
2015 Jan 01	57023.52876	3000	1.16	cloudy, 1″	6	9.7 ± 1.8	28.4 ± 1.7[b]
2015 Dec 29	57385.54397	3000	1.16	clear, 0.″5	22	17.5 ± 0.4	39.0 ± 0.7
2016 Jan 18	57405.48029	3000	1.18	clear, 0.″5	16	17.5 ± 0.5	36.1 ± 0.9
2016 Feb 03	57421.40203	2800	1.13	clear, 1″–2″	15	17.8 ± 0.6	35.4 ± 1.0
2016 Feb 16	57434.32974	2400	1.15	clear, 0.″6	22	16.3 ± 0.7	37.2 ± 0.5
2016 Apr 22	57500.25885	2400	1.20	clear, 0.″5	15	14.7 ± 0.5	39.0 ± 0.8

Notes.
[a] Additional systematic errors of 2.5 km s^{-1} for these parameters are not included in the values listed here.
[b] These values were not included in the computation of the mean $V_{rot} \sin i = 34.1 \pm 0.7$ km s^{-1}; see Section 4.

orbital mass measurements and component atmospheric characterization (Bardalez Gagliuffi et al. 2015).

One of these systems is SDSS J080531.84+481233.0 (hereafter SDSS J0805+4812), a peculiar L dwarf identified in the Sloan Digitial Sky Survey (SDSS York et al. 2000) that exhibits highly divergent optical (L4; Hawley et al. 2002) and near-infrared (L9.5, Knapp et al. 2004) spectral classifications. It was identified as a potential L dwarf plus T dwarf binary on the basis of its spectral peculiarities (Burgasser 2007), and found to be an astrometric variable by Dupuy & Liu (2012) with an amplitude of ≈15 mas. While unable to constrain the orbit of the system, Dupuy & Liu (2012) estimated a semimajor axis of 0.9–2.3 au and orbital period of 2.7–9.1 years, but found no evidence of a resolved companion in unpublished observations with Keck Laser Guide Star Adaptive Optics (LGSAO; van Dam et al. 2006; Wizinowich et al. 2006) observations. Bardalez Gagliuffi et al. (2015) have also reported this source as unresolved in two epochs of Keck LGSAO imaging with an angular separation upper limit of 170 mas, taking into account the expected flux ratio of the system.

In this article, we report the detection of significant and periodic radial velocity variations in high-resolution spectroscopic monitoring of SDSS J0805+4812 that allow us to make the first robust constraints on the orbital and physical properties of the system components. In Section 2 we describe the observations and data analysis methodology that yield both radial and rotational velocities for the source. In Section 3 we update the spectral characterization of the SDSS J0805+4812AB components through a revised analysis of its combined-light near-infrared spectrum. In Section 4 we briefly describe our orbital analysis and determination of the system parameters, including constraints based on the component spectral types and evolutionary models. We discuss our results in Section 5. A detailed description of our spectral analysis and orbital modeling are provided in the Appendices.

2. OBSERVATIONS AND DATA ANALYSIS

High resolution near-infrared spectra of SDSS J0805+4812 were obtained with the Near InfraRed SPECtrometer (NIRSPEC; McLean et al. 2000) on the Keck II telescope over 14 epochs between 2012 April 02 and 2016 April 22 (Table 1). In all cases, data were acquired using the N7 order-sorting filter and 0.″432-wide slit to obtain 2.00–2.39 μm spectra over orders 32–38 with $\lambda/\Delta\lambda \approx 20{,}000$ ($\Delta v \approx 15$ km s^{-1}) and dispersion of 0.315 Å pixel^{-1}. For each observation, two exposures of 1200–1500 s each were obtained, nodding 7″ along the slit, followed by observations of the nearby A0 V star HD 71906 ($V = 6.18$) at a similar airmass. Flat field and dark frames were obtained at the start of each night for detector calibration.

We improved upon the forward-modeling process described in Burgasser et al. (2015) by incorporating an iterative, multithreaded Markov Chain Monte Carlo (MCMC) algorithm to achieve more consistent results across observations; our methodology is detailed in Appendix A. Figure 1 illustrates a sample extraction and fit from our 2016 February 16 (UT) observations, and the resulting

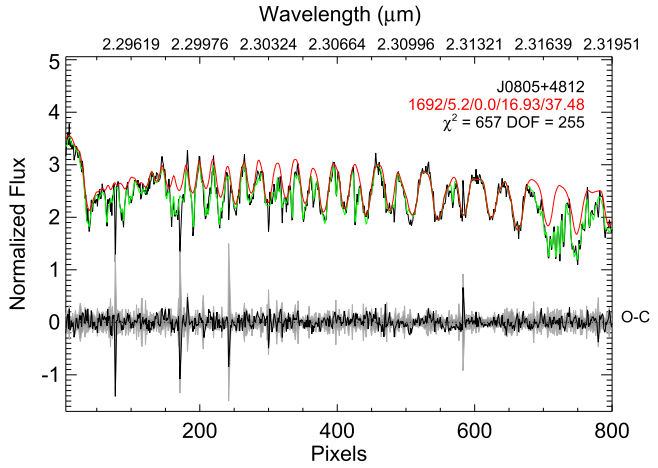

Figure 1. NIRSPEC order 33 spectrum of SDSS J0805+4812 obtained on UT 2016 February 16 (black line), compared to the best-fit interpolated atmosphere model from Allard et al. (2012, red line), parameterized as $T_{eff} = 1692$ K, $\log g = 5.2$, [M/H] ≡ 0, RV = 16.93 km s^{-1} and $V_{rot} \sin i = 37.48$ km s^{-1}. The best-fit model times scaled telluric absorption is shown as the green line. Pixel scale is listed along the bottom while wavelength scale is listed along the top. The difference between data and model (O–C) is shown in black at the bottom of the plot; the ±1σ uncertainty spectrum is indicated in gray. The $\chi^2 = 657$ and 255 degrees of freedom (dof) indicate a reasonable fit.

radial and rotational velocities for all epochs analyzed are listed in Table 1. The median signal-to-noise ratio (S/N) of the extracted data in order 33 (2.29–2.33 μm) ranged from 6 to 23. Measured uncertainties spanned 0.3–1.8 km s^{-1} for radial velocities and 0.4–1.8 km s^{-1} for rotational velocities, in line with spectral S/N. We infer an additional systematic uncertainty for the rotational velocities of 2.5 km s^{-1} by enforcing consistency in the measurements ($P(\chi^2, \mathrm{dof}) < 90\%$)[5] over eleven epochs, excluding the S/N < 10 data from 2015 December 8 and 2016 January 1 (UT). The uncertainty-weighted mean rotational velocity is 34.1 ± 0.7 km s^{-1}, with no significant correlation between radial and rotational velocities. Assuming a radius of 0.084 $R_\odot$, based on the evolutionary models of Baraffe et al. (2003) for an effective temperature $T_{\rm eff}$ = 1700 K and age of 4 Gyr (see below), this projected velocity translates into a maximum rotational period of 3.0 hr. Like many mid-type L dwarfs, SDSS J0805+4812A is a rapidly rotating dwarf which nevertheless lacks magnetically driven nonthermal Hα emission (Hawley et al. 2002).

The radial velocities are inconsistent with a constant value ($\chi^2 = 368$, dof = 13) and display periodic variation. We interpret this behavior as the reflex motion of the primary under the gravitational influence of a brown dwarf secondary, and use these data to infer the orbit of the system as described below.

3. RE-EXAMINATION OF THE SPECTRAL COMPOSITION OF SDSS J0805+4812

The initial identification of SDSS J0805+4812AB as a spectral binary candidate was based on comparison of its blended-light spectrum with 50 L and T dwarf templates. That analysis inferred component types of L4.5 and T5. Dupuy & Liu (2012), using a similar technique, inferred equivalent classifications of L5: and T5. We revisited these analyses following the procedures described in Burgasser et al. (2010), comparing the SpeX spectum of SDSS J0805+4812 to 534 L2–T8 spectral templates from an updated SpeX Prism Library (Burgasser 2014), and 76,873 binary templates constructed from these templates after scaling them to absolute magnitudes using the Dupuy & Liu (2012) M_J/spectral type relation. The best-fit spectral binary template, composed of the L3.5 2MASS J0036159+182110 (Reid et al. 2000) and the T4.5 SDSS J083048.80+012831.1 (Knapp et al. 2004) is shown in Figure 2. F-test statistic-weighted means from the best 100 fits (lowest χ^2) yield decimal component types of L4.2 ± 0.7 and T5.5 ± 1.1, consistent with prior determinations. We use these component types and their uncertainties in our analysis of the orbital properties of the system below.

4. DETERMINING THE ORBIT OF SDSS J0805+4812AB

We analyzed the radial velocity curve of SDSS J0805+4812 using an improved MCMC orbit-fitting code based on Burgasser et al. (2015) and described in detail in Appendix B. Two separate fits were made to the data: an "unconstrained" fit with a weak limit on the total mass of the system ($M_{\rm tot} \leqslant 0.3\,M_\odot$) and a "constrained" fit in which the orbit-deduced component and total system masses were compared to predictions from evolutionary models and component effective temperatures, following Burgasser & Blake (2009). The temperatures were estimated from several

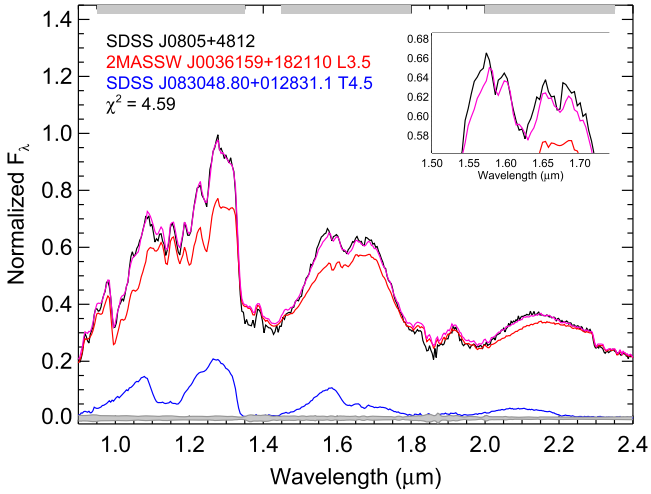

Figure 2. Best-fit spectral binary template (purple line) compared to the combined-light SpeX spectrum of SDSS J0805+4812 (black line). The template is composed of the L3.5 2MASS J0036159+182110 (red linel data from Burgasser et al. 2008) and the T4.5 SDSS J083048.80+012831.1 (blue line; data from Burgasser et al. 2010), both shown at their relative scaling. The gray bars at top indicate the regions over which the fitting was done. The ±1σ uncertainty spectrum of SDSS J0805+4812 is shown in gray along the bottom. The inset box highlights the 1.50–1.75 μm range where the "dip" feature is seen, arising from overlapping FeH and CH_4 absorption from pimary and secondary, respectively.

$T_{\rm eff}$/spectral type relations (Golimowski et al. 2004; Looper et al. 2008; Stephens et al. 2009; Marocco et al. 2013; Filippazzo et al. 2015), yielding 1650–1825 K for SDSS J0805+4812A and 990–1140 K for SDSS J0805+4812B, with uncertainties[6] of 100–150 K. We converged on average values of 1740 ± 100 K and 1070 ± 80 K. These temperatures were converted to age-dependent masses using the solar-metallicity models of Baraffe et al. (2003). Figure 3 displays the component and total system masses as a function of age, as well as the mass function

$$f_M^{(\rm evol)} = \frac{M_2}{(M_1 + M_2)^{2/3}}. \quad (1)$$

These parameters were used to restrict solutions in the constrained orbit fit. We determined that an additional 0.5 km s^{-1} systematic uncertainty in the radial velocity measurements is required based on the χ^2 of the best-fit orbit models.

Figures 4 and 5 show the best-fit orbits from both analyses, while Figures 6 and 7 display the distributions and correlations for P, a, e, i, q and $M_{\rm tot}$ from the MCMC chains. Table 2 lists the best-fit and mean orbital parameters and inferred component properties. The χ^2 values for the best-fit solutions in both the constrained and unconstrained fits indicate convergence, and both analyses produce nearly identical values for the period (2.02 ± 0.03 years), eccentricity (0.46 ± 0.05), inclination[7] (90° ± 19°) and center-of-mass radial velocity (10.8 ± 0.3 km s^{-1}). The remaining orbital values are also statistically consistent between the analyses. We verified that the period, an integer multiple of a year, was not the result of phased sampling; the opposing phase of our 2013 and 2016 February measurements assures this.

While the two analyses yield equivalent orbital parameters, they make notably different predictions for the inferred

[5] $P(\chi^2, \mathrm{dof})$ is the probability distribution function of the χ^2 distribution for degrees of freedom (dof) equal to the number of measurements N minus one. We use the standard defintion of $\chi^2 = \sum_i^N \frac{(m_i - \bar{m})^2}{\sigma_i^2}$, where m_i are the measured values, $\bar{m}$ the uncertainty-weighted mean, and σ_i the measurement uncertainties.

[6] Uncertainties include the spectral type uncertainties and systematic uncertainties in the relations.

[7] In this analysis, orbital inclinations <90° correspond to clockwise orbital motion, >90° to counterclockwise motion, as projected on the sky.

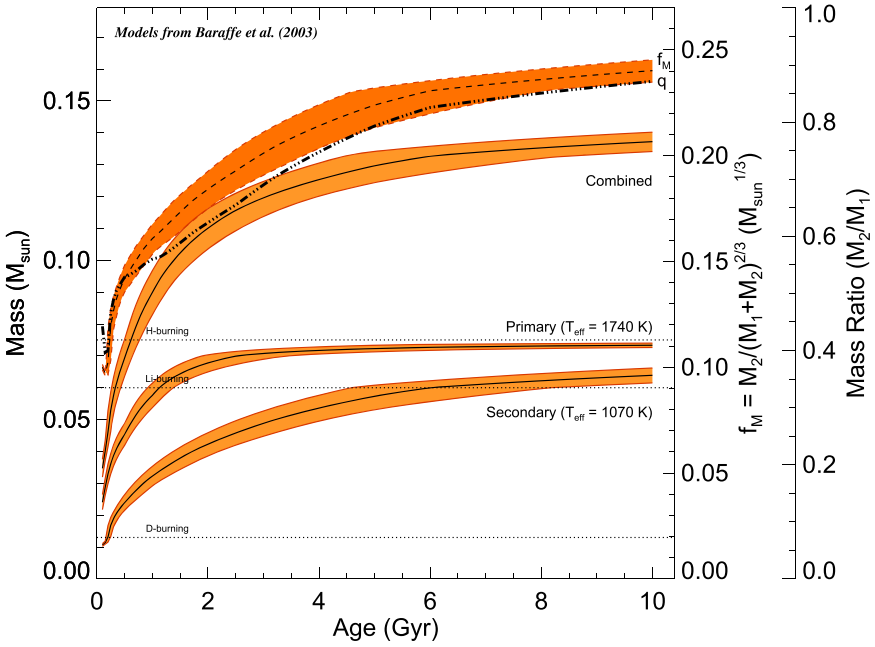

Figure 3. Estimated component and combined masses of SDSS J0805+4812A and B as a function of system age (solid lines) based on their estimated L4 ± 0.7 and T5.5 ± 1.1 classifications, corresponding $T_{\rm eff}$ estimates of 1740 ± 100 K and 1070 ± 80 K, respectively; and the evolutionary models of Baraffe et al. (2003). The dashed line shows the corresponding mass function, $f_M = M_2/(M_1 + M_2)^{2/3}$ (near right axis), while the triple-dot dash line shows the mass ratio $q = M_2/M_1$ (far right axis). The deuterium, lithium and hydrogen burning minimum-mass limits are labeled as dotted lines.

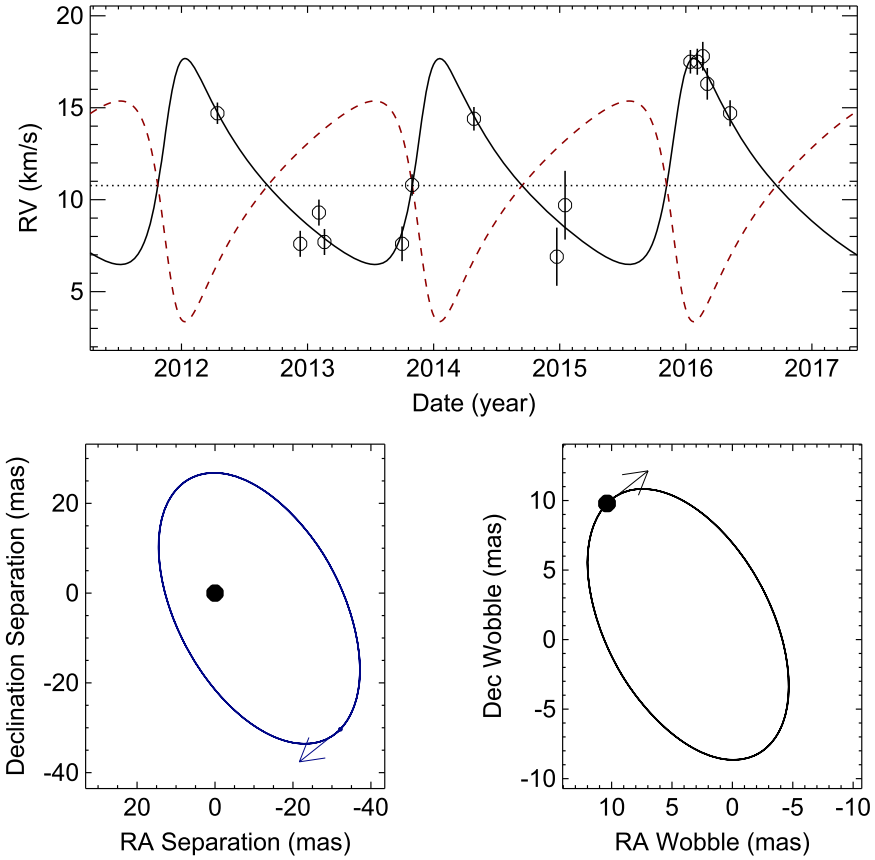

Figure 4. Best-fit (minimum χ^2) orbital solution from MCMC orbital analysis of NIRSPEC data, unconstrained by evolutionary models. The top panel shows the predicted radial motion of both the primary (solid black line) and secondary (red dashed line) as compared to primary radial velocity measurements (open circles with error bars). The bottom left panel shows the predicted orbital motion of the secondary (blue line) relative to the primary (black dot at the origin) projected on the sky. The bottom right panel shows the predicted astrometric orbital motion of the primary (distinguished from parallactic motion) projected on the sky. In the bottom panels, the arrow indicates the direction of orbital motion (secondary or primary) at apoapsis, and the orbits are shown at an arbitrary longitude of ascending node, which is unconstrained in these observations. Parameters for these fits are listed in Table 2.

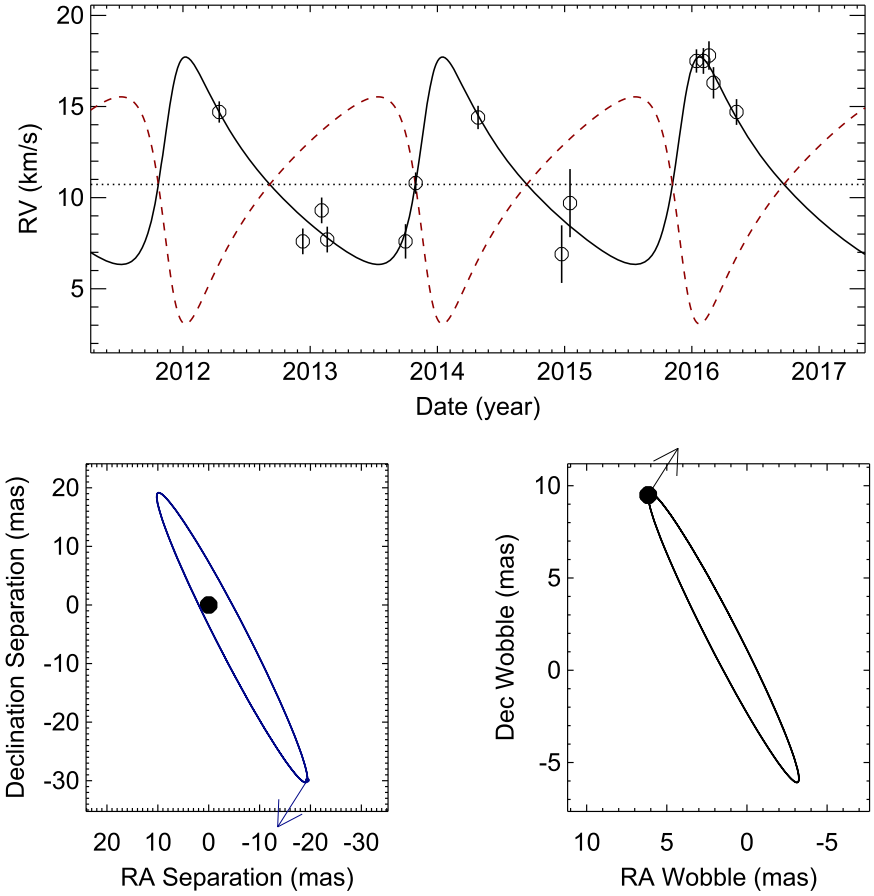

Figure 5. Same as Figure 4 but based on fits constrained by evolutionary models.

component properties of this system. The unconstrained fit favors larger values for the component and total system masses, predicting in particular a likely stellar mass for SDSS J0805+4812A and a mass at the hydrogen-burning limit for SDSS J0805+4812B. In contrast, the constrained fit is limited to a total mass of $0.14\,M_{\odot}$, and predicts masses for both components that are likely to be below the hydrogen burning limit. These distinctions are discussed in Section 5.

Returning to the orbital parameters, one striking feature of the fits is that an edge-on orbital inclination is favored, albeit with large uncertainties. This orientation is necessary for the constrained fit to reproduce the large radial velocity amplitude of the primary given the (model predicted) substellar masses of the components. Requiring that the observed system mass function not exceed the maximum limit inferred from the evolutionary models, we determine a minimum system inclination of $63^{\circ}{}^{+10^{\circ}}_{-8^{\circ}}$ (Figure 8). This analysis also predicts a minimum age for the SDSS J0805+4812 system of $4.0^{+1.9}_{-1.2}$ Gyr, again necessary to have a large enough secondary mass to reproduce the observed reflex motion of the primary. We reiterate that these values are model-dependent, and also dependent on correct estimation of the component effective temperatures. Large inclinations and system ages were previously obtained in analyses of the spectral binaries 2MASS J03202839–446358AB ($i \gtrsim 53^{\circ}$, $\tau \gtrsim 2$ Gyr; Burgasser & Blake 2009) and SDSS J000649.16–085246.3 ($i \gtrsim 61^{\circ}$, $\tau \gtrsim 4$ Gyr; Burgasser et al. 2012). The similarity in these results is likely a selection effect. Given the sensitivity limits to radial velocity variations for these low-mass and low-luminosity sources, older, more edge-on systems are more detectable as variables than younger and/or lower inclination systems.

Finally, we note that the predicted astrometric orbits for the best-fit cases are consistent with prior measurements of the system. The separation between primary and secondary as projected on the sky does not exceed 50 mas, well within the resolution limits of previously published LGSAO observations. The astrometric wobble of the primary, assuming a relative magnitude of $\Delta J = 1.8$ mag based on the spectral template analysis above, has a maximum amplitude of roughly 15 mas, consistent with the astrometric residuals reported by Dupuy & Liu (2012).

5. DISCUSSION

The combined detection of astrometric and radial velocity variability unambiguously confirms SDSS J0805+4812 as a VLM binary system. Our measurements of the primary radial motion yield stringent constraints on the orbital period (1.4%), system velocity (3%), eccentricity (5%), and semimajor axis (8%); and a reasonable constraint on the system mass ratio (12%) which is coupled to other parameters (a and $M_{\rm tot}$) and partly dependent on the atmosphere models. The inferred system and component masses are much more weakly constrained (20%–30%), strongly correlated with other parameters (e.g., q), and highly sensitive to inputs from the evolutionary models. As such, our orbit parameter determinations are insufficient to directly test the models.

There are additional observables that could be brought to bear on this problem, however. The inferred primary mass is

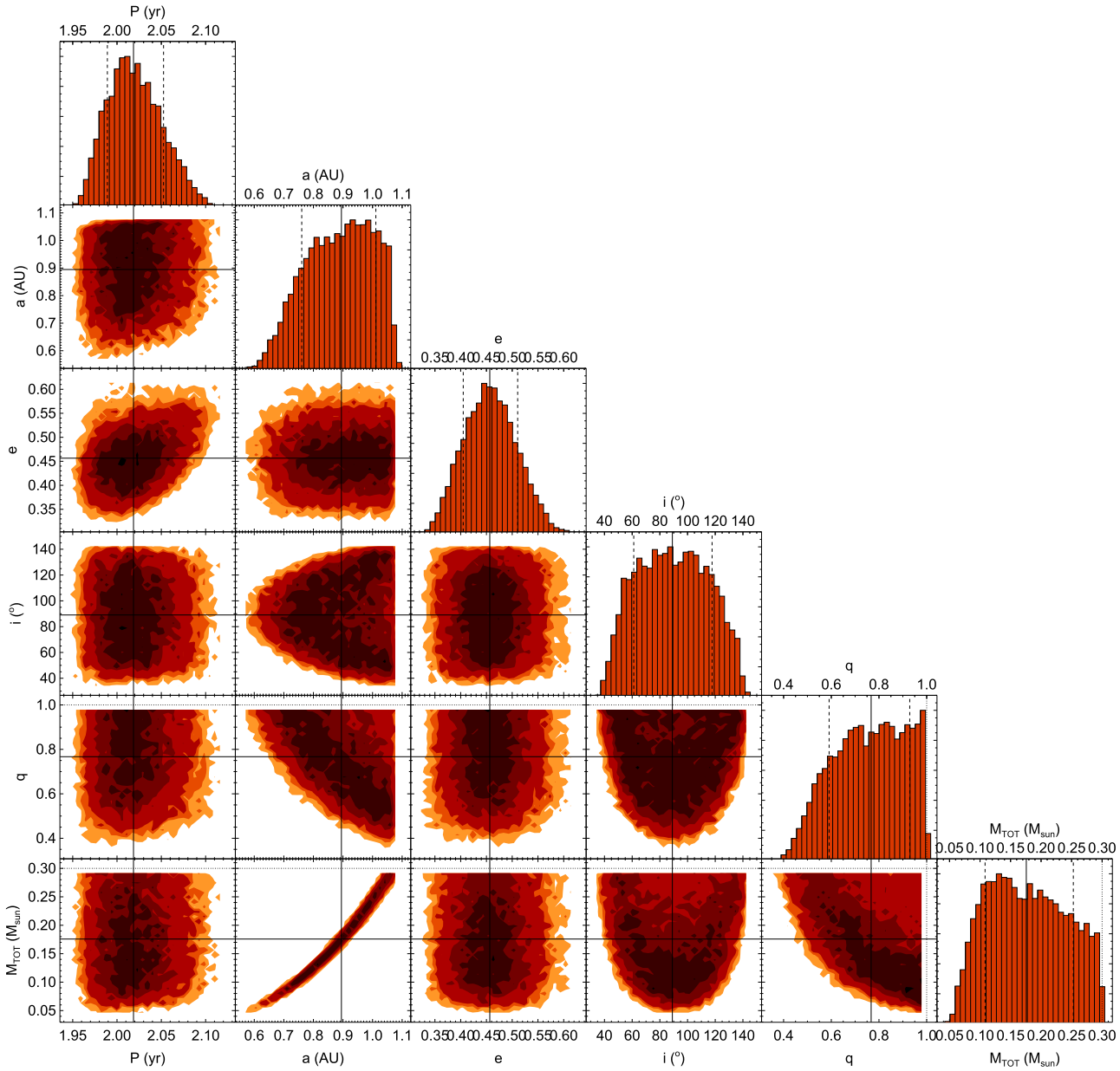

Figure 6. Parameter distributions and correlations (triangle plot) for period (P), semimajor axis (a), eccentricity (e), inclination (i), mass ratio (q) and total system mass ($M_{\rm tot}$) based on our MCMC orbital fit of the primary radial velocity data without constraints imposed by the evolutionay models. The fits assume weak constraints on period (0.2 year $\leqslant P \leqslant$ 30 year), eccentricity ($e \leqslant 0.95$) and total mass ($M_{\rm tot} \leqslant 0.3\ M_{\odot}$; dotted lines in histograms). Contour plots show two-dimensional frequency distributions for parameter pairs, highlighting correlations (e.g., a and $M_{\rm tot}$, q and $M_{\rm tot}$). Normalized histograms at the ends of rows are marginalized over all other parameters. Median values are indicated by solid lines in all panels; 16% and 84% quantiles are indicated by dashed lines in the histograms. These values are listed in Table 2.

either below or above the lithium-burning minimum mass limit of $0.060\,M_{\odot}$ (Bildsten et al. 1997; Ushomirsky et al. 1998), depending on whether the orbit fits are constained by evolutionary models or not. The Li I absorption line at 6708 Å is readily detectable in the optical spectra of early- and mid-type L dwarfs; however, previously reported spectral data of SDSS J0805+4812 do not have sufficient S/N to assess the presence of this feature. New observations to apply the "lithium test" on this system (Magazzu et al. 1991; Martin et al. 1994; Liu & Leggett 2005) may considerably constrain the allowed parameter space for its orbit, or indicate disagreement between the evolutionary models and orbital parameters. A more direct measure of the mass ratio could also be made from the reflex motion of the secondary, whose signal is buried within the combined light spectrum of the system. Analysis methods such as TODCOR (Mazeh & Zucker 1994) could be employed to extract this signal in spectral regions where the secondary contributes a greater fraction of the total flux, such as the 1.25–1.30 μm J-band and 1.55–1.60 μm H-band psuedo-continuum peaks of T dwarfs. These observations are currently proposed and will be examined in a future study.

Despite the accuracy obtained for the orbital elements P, a and e, further observations to more tightly constrain the orbit geometry are warranted. Of particular interest is inclination, as the rapid rotation of SDSS J0805+4812A inferred from these measurements makes this an ideal system to explore spin–orbit

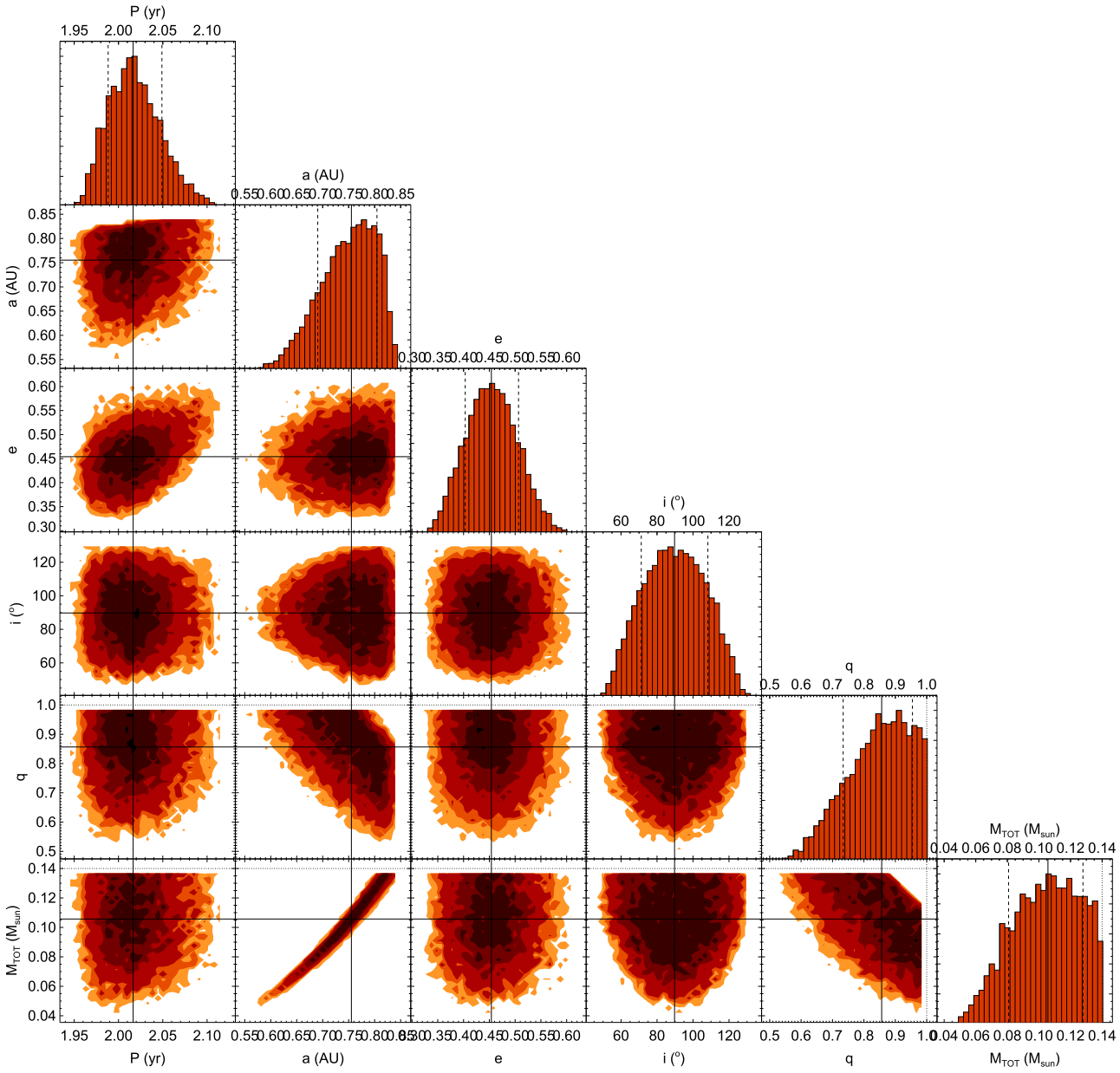

Figure 7. Same as Figure 6 but with orbit models constrained by evolutionary models.

alignment in VLM star-brown dwarf multiples. To date, only a single VLM stellar pair, the L0+L1.5 2MASSW J0746425 +200032AB (Reid et al. 2000, 2001; Bouy et al. 2003, 2004) has been tested and confirmed to be in alignment to within 10° (Harding et al. 2013). Improving the constraint on the inclination of SDSS J0805+4812AB to within this limit, and measuring a robust rotation period through photometric variability,[8] would permit a similar test of alignment based on an assumed radius, or a radius determination for SDSS J0805+4812A assuming alignment. Combining our radial velocity measurements with prior or concurrent measurements of astrometric variability should in principle improve orbital parameters, as well as yield a measure of the longitude of ascending node which is unconstrained in these data. While a direct view of the orbit has so far proven too challenging for LGSAO direct imaging, sparse-aperture mask imaging with AO (Tuthill et al. 2006) may be a useful alternative approach. Prior work has demonstrated that companions with contrast ratios of $\Delta m \gtrsim 3$, appropriate for *K*-band imaging of SDSS J0805+4812AB, can be resolved for separations $\gtrsim$20 mas with Keck NIRC2 LGSAO (Burgasser et al. 2008; Kraus et al. 2008). This is sufficient to resolve the system at apoapsis, and would again aid in constraining the overall orientation of the orbit.

The semimajor axis of this system falls well below the peak of the separation distribution of the current sample of known VLM multiples, ~4 au (Allen 2007; Bardalez Gagliuffi et al. 2014, 2015). Since this sample is dominated by sources uncovered through resolved imaging, our result is not particularly surprising. However, it does add to growing evidence that tight separations are common among confirmed

[8] Khandrika et al. (2013) reported no variability in two monitoring epochs of 2 hr each to a limiting amplitude of 3% in both *J*- and *K*-band observations; however, this limit is comparable to the amplitudes of known VLM variables (Radigan et al. 2012).

Table 2
Parameters from Orbital Analysis

Parameter	Without Evolutionary Model Constraints		With Evolutionary Model Constraints	
	Best-fit	Median	Best-fit	Median
Modeled Parameters				
Best χ^2 (dof)	10.3 (7)	…	10.1 (7)	…
P[a] (year)	2.02	$2.02^{+0.03}_{-0.03}$	2.02	$2.02^{+0.03}_{-0.03}$
a (au)	0.85	$0.89^{+0.12}_{-0.13}$	0.72	$0.76^{+0.05}_{-0.06}$
e[a]	0.45	$0.46^{+0.05}_{-0.05}$	0.45	$0.46^{+0.05}_{-0.05}$
i (°)	125	89^{+29}_{-28}	96	90^{+19}_{-19}
ω (°)	301	304^{+16}_{-15}	300	308^{+15}_{-14}
M_0 (°)	68	66^{+13}_{-14}	70	63^{+13}_{-14}
q	0.93	$0.77^{+0.16}_{-0.18}$	0.91	$0.86^{+0.10}_{-0.12}$
$V_{\rm COM}$ (km s^{-1})	10.8	$10.7^{+0.3}_{-0.3}$	10.7	$10.8^{+0.3}_{-0.3}$
Inferred Parameters				
$M_{\rm tot}$ ($M_\odot$)	0.15	$0.18^{+0.08}_{-0.07}$	0.09	$0.11^{+0.02}_{-0.02}$
M_1 ($M_\odot$)	0.079	$0.10^{+0.05}_{-0.04}$	0.048	$0.057^{+0.016}_{-0.014}$
M_2 ($M_\odot$)	0.074	$0.07^{+0.03}_{-0.02}$	0.044	$0.048^{+0.008}_{-0.010}$
K_1 (km s^{-1})	5.6	$5.6^{+0.6}_{-0.5}$	5.7	$5.4^{+0.4}_{-0.4}$
K_2 (km s^{-1})	6.0	$7.4^{+2.1}_{-1.4}$	6.2	$6.4^{+1.0}_{-0.8}$
Minimum Age (Gyr)	…	…	4.2	$4.0^{+1.9}_{-1.2}$
Minimum Inclination (°)	…	…	64	63^{+10}_{-8}

Note.
[a] Parameter was constrained to a limited value range in MCMC analysis.

VLM spectral binary systems, whose identification is independent of separation up to ∼500 mas (10 au at 20 pc). These results suggest that many other VLM systems without the necessary spectral composition to be detected as spectral binaries may be currently overlooked. Ongoing radial velocity monitoring, astrometric monitoring and high-resolution imaging of spectral binary candidates will provide a more robust assessment of the close-separation binary fraction, and a pathway toward accurate determination of the overall binary fraction of the coolest stars and brown dwarfs.

The authors thank Joel Aycock, Scott Dahm, Randy Campbell, Greg Doppman, Heather Hershey, Carolyn Jordan, Marc Kassis, Jim Lyke, Gary Punawai, Julie Rivera, Terry Stickel, Hien Tran, and Cynthia Wilburn at Keck Observatory, and Christine Nichols and Melisa Tallis at UCSD, for their assistance with the NIRSPEC observations. AJB acknowledges funding support from the National Science Foundation under award No. AST-1517177. The material is based upon work supported by the National Aeronautics and Space Administration under Grant No. NNX15AI75G. This research has made use of the SIMBAD database, operated at CDS, Strasbourg, France; NASA's Astrophysics Data System Bibliographic Services; the M, L, T, and Y dwarf compendium housed at DwarfArchives.org; and the SpeX Prism Libraries at http://www.browndwarfs.org/spexprism. We thank our anonymous referee for her/his/their prompt and helpful review of the original manuscript. The authors recognize and acknowledge the very significant cultural role and reverence that the summit of Mauna Kea has always had within the indigenous Hawaiian community. We are most fortunate and grateful to have the opportunity to conduct observations from this mountain.

APPENDIX A
FORWARD MODELING OF THE NIRSPEC SPECTRA

To accurately determine radial and rotational velocities from the NIRSPEC data, we adapted the forward-modeling procedure described in Burgasser et al. (2015), which is in turn based on the method described in Blake et al. (2010). Data were initially reduced and rectified using a modified version of the REDSPEC package, and source and A0 standard spectra in order 33 (2.29–2.33 μm) optimally extracted, scaled and co-added with uncertainty weighting. Spectral uncertainties (σ) were determined from image variance, a combination of Poisson shot noise, read noise (50 e$^-$; Blake et al. 2010) and variance between the individual extractions.

These "raw" spectra are a function of pixel position and include telluric absorption and residual pixel sensitivity variations. Rather than calibrate these effects, we followed an iterative forward-modeling approach using a multi-threaded MCMC method with a Metropolis–Hasting algorithm (Metropolis et al. 1953; Hastings 1970). The extracted data were modeled as

$$D[p(\lambda)] = C[p(\lambda)] \times \left[\left(M\left[p\left(\lambda\left[1+\frac{\rm RV}{c}\right]\right)\right]\right) * \kappa_R(V_{\rm rot}\sin i))T[p(\lambda)]^{\alpha}\right] * \kappa_G(\Delta v_{\rm inst}). \quad (2)$$

Here, $p(\lambda)$ is the wavelength-to-pixel translation, which was modeled as a second-order polynomial; $C[p]$ is a continuum correction, also modeled as a second-order polynomial; $M[p]$ is a solar-metallicity BT-Settl atmosphere model (Allard et al. 2011) parameterized by $T_{\rm eff}$ and $\log g$, used to represent the spectrum of SDSS J0805+4812; the model spectrum is wavelength-shifted by the radial velocity RV; $T[p]$ is the telluric transmission spectrum from the Solar atlas of Livingston & Wallace (1991); α is the telluric transmission scaling factor; and κ_R and κ_G are the rotational and instrumental broadening profiles convolved ($*$) with the model spectrum, which are parameterized by the projected rotational velocity $V_{\rm rot}\sin i$ and a Gaussian with velocity width $\Delta v_{\rm inst}$, respectively.

The full model contains 12 parameters, but not all were fit simultaneously. We first determined the wavelength-to-pixel translation and instrumental broadening using our calibration observations. This mapping was first estimated by comparing the arc lamp spectrum to line air wavelengths as compiled by the National Institute of Standards and Technology (NIST Atomic Line Database; Kramida et al. 2014). We then fit the telluric absorption spectrum of the otherwise featureless A0 V star ($M[p] = 1$), iteratively fitting residuals in cross-correlations between the Solar telluric atlas and the extracted telluric spectrum over narrow (30 pixel = 0.001 μm) spectral regions to converge on the wavelength solution. Typical residuals were (0.7–1.0) × 10^{-6} μm (∼0.1 km s^{-1}). The instrumental broadening was also determined at this step to be in the range 4.6–5.0 pixels ($\Delta v_{\rm inst}$ = 19–21 km s^{-1}). An example fit from data on 2016 February 16 (UT) is shown in Figure 9.

The spectrum of SDSS J0805+4812AB was fit in three separate passes. First, fixing the instrumental broadening and first- and second-order coefficients for the wavelength solution,

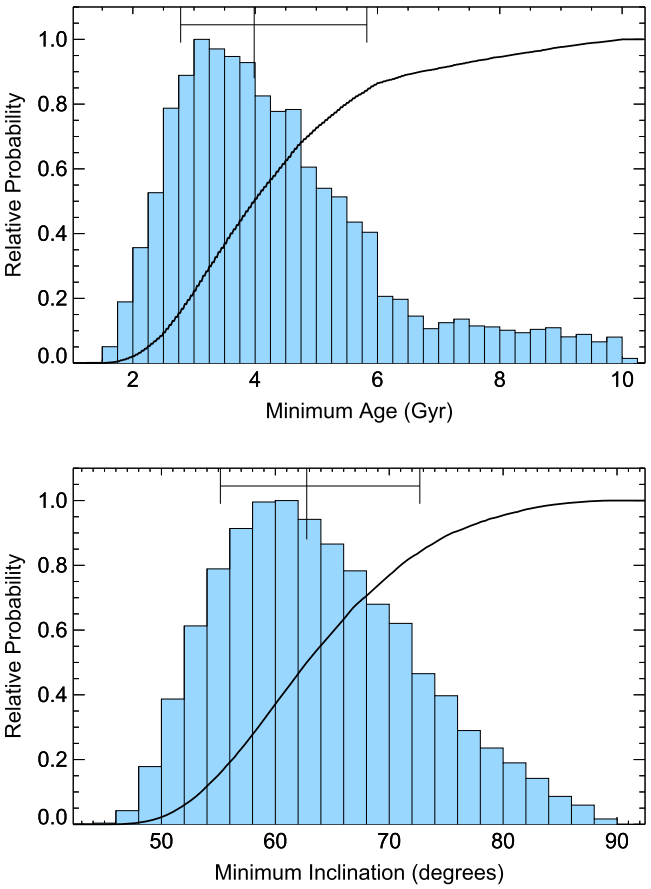

Figure 8. Constraints on the minimum age (top panel) and minimum orbital plane inclination (bottom panel) of the SDSS J0805+4812AB system, assuming limits imposed by the evolutionary models. The histograms show the distributions of these values for all viable orbits in the MCMC chain; the error bars at top indicates the median and 16% and 84% quantiles of the distributions (listed in Table 2). Red lines trace the cumulative distributions.

the four parameters RV, $V_{\rm rot}\sin i$, α and the zeroth-order coefficient in the wavelength-to-pixel translation, as well as the three coefficients for the continuum correction, were determined by MCMC analysis using a $T_{\rm eff} = 1700$ K, $\log g = 5.0$ cgs model and initial estimates RV $= 0$ km s^{-1} and $V_{\rm rot}\sin i = 30$ km s^{-1}. A single MCMC chain of length 8,000 steps was used (2000 per parameter), with parameters sequentially updated (Gibbs sampling) by drawing offsets from normal distributions with predetermined widths (generally ~10 times larger than the final uncertainties). A chi-square statistic was used to compare data ($d[p]$) to model ($D[p]$)

$$\chi^2 = \sum \frac{(d[p] - D[p])^2}{\sigma[p]^2}. \quad (3)$$

A new parameter set $\boldsymbol{\theta}(i) \rightarrow \boldsymbol{\theta}(i+1)$ was adopted if the acceptance condition $U(0, 1) \leqslant e^{-0.5(\chi^2(i+1)-\chi^2(i))}$ was satisfied, where $U(0, 1)$ is a random draw from a uniform distribution between 0 and 1. The effective degrees of freedom of this fit was estimated as (number of data pixels)/3—(number of fit parameters) ≈250. The scale factor of 3 pixels roughly accounts for correlated data due to instrumental line broadening. Note that the coefficients for the continuum correction function were not iterated in this manner, but determined instead by fitting a second-order polynomial to the ratio of model and observed spectrum at

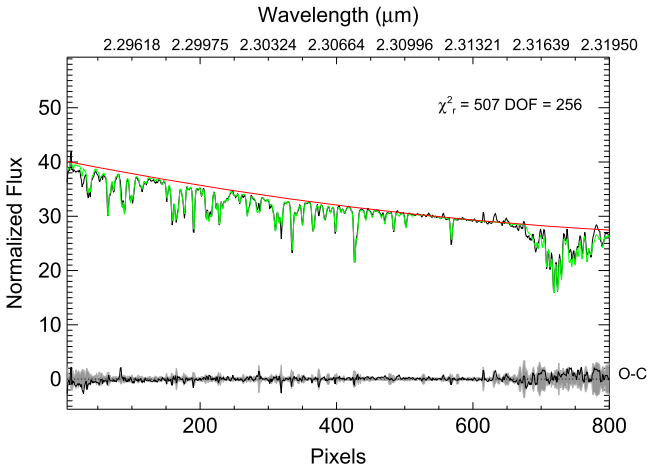

Figure 9. Fit to the spectrum of the A0 V telluric calibrator HD 71906 observed on 2016 February 16 (UT). The extracted spectrum is shown in black; the (featureless) A0 V continuum, modeled as a second-order polynomial, is shown in red; and the full model, including scaled telluric absorption, is shown in green. Residuals are plotted as the gray line around zero, and is dominated by uncorrected fringing. Pixel scale is listed along the bottom while wavelength scale is listed along the top.

each step. After this initial chain, these parameters were fixed and the data then compared to a suite of BT-Settl models spanning $T_{\rm eff} = 1500$–2500 K in steps of 100 K and $\log g = 4.0$–5.5 (cgs) in steps of 0.5 dex, again using the χ^2 statistic and fitting the continuum separately. The best-fit atmosphere model from this analysis, typically $T_{\rm eff} = 1900$–2100 K and $\log g = 5.0$–5.5, was then used as the starting point of a multi-threaded MCMC analysis for which 9 parameters (RV, $V_{\rm rot}\sin i$, α, $T_{\rm eff}$, $\log g$, the zeroth-order wavelength coefficient, and the three continuum coefficients) were fit iteratively. We used an implementation of the Goodman & Weare (2010) affine-invariant MCMC ensemble with $N_C = 10$ independent chains, each with initial conditions drawn from uniform distributions centered on the best-fit values from the first two fitting passes and widths at least three times the standard deviation of these passes. Models with intermediate values of $T_{\rm eff}$ and $\log g$ were linearly interpolated in logarithmic flux between the model grid nodes. The chains were evolved for $N_S = 12{,}000$ steps following the same Metropolis–Hastings algorithm as above.

Figure 10 shows the chain evolution for the parameters RV, $V_{\rm rot}\sin i$, $T_{\rm eff}$ and $\log g$ for our fit to the 2016 February 16 (UT) data, while Figure 11 compares the resulting distributions of these parameters based on the last 75% of all chains. The chains for RV and $V_{\rm rot}\sin i$ converge quickly to common values, and convergence was quantified for all parameters by computing the Gelman & Rubin (1992) scale reduction factor for each parameter θ_j,

$$\hat{R}_j = \frac{N_S - 1}{N_S} + \frac{N_C + 1}{N_S N_C}\frac{B_j}{W_j}\frac{\rm dof}{\rm dof - 2} \quad (4)$$

where

$$W_j = \frac{1}{N_C}\sum_{i=1}^{N_C}(\theta_{ij} - \bar{\theta}_{ij})^2 \quad (5)$$

$$B_j = \frac{N_S}{N_C - 1}\sum_{i=1}^{N_C}(\bar{\theta}_{ij} - \bar{\theta}_j)^2 \quad (6)$$

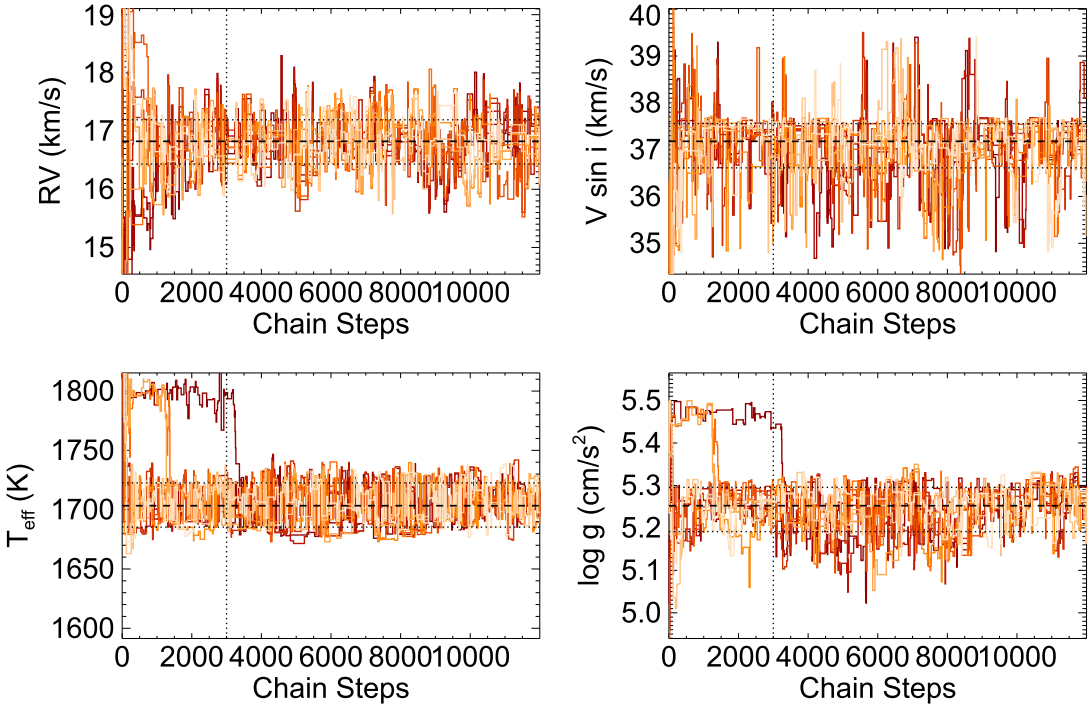

Figure 10. MCMC chains for fit parameters RV, $V_{\rm rot}\sin i$, $T_{\rm eff}$ and $\log g$ for data taken on 2016 February 16 (UT). The best-fit spectrum is shown in Figure 1. Chain values to the left of the dotted lines were not included in the parameter distributions and estimates.

are the average within-chain variances and variance in the between-chain means, respectively.[9] For RV, $V_{\rm rot}\sin i$, and the other fitting parameters, we confirmed that $\hat{R} < 1$, indicating that the well-sampled prior distribution converged to a common posterior distribution. The model parameters $T_{\rm eff}$ and $\log g$, on the other hand, converged more slowly and, in some cases, to distinct, discrete values for different chains indicating that these parameters are not properly converged. We find minimal correlation between these model parameters and RV and $V_{\rm rot}\sin i$ (Figure 11), so we did not attempt to address this issue, and defer discussion for a future study. The best-fit and mean parameters and their uncertainties for all epochs are summarized in Table 3.

APPENDIX B
ORBIT FITTING ANALYSIS

The primary radial velocity orbit of SDSS J0805+4812AB was inferred using an adaptation of the MCMC analysis described in Burgasser et al. (2012, 2015). We examined a two-component orbit model with seven parameters,

$$\boldsymbol{\theta} = (P,\ a,\ e,\ i,\ \omega,\ M_0,\ q,\ V_{\rm COM}) \tag{7}$$

where P is the period of the orbit in years, a is the semimajor axis in au, e is the eccentricity, i is the inclination, ω is the argument of periastron, M_0 is the mean anomaly at epoch $\tau_0 = 2012.253$ (MJD[10] $= 56019.28665$), $q \equiv M_2/M_1$ is the system mass ratio, and $V_{\rm COM}$ is the center of mass (systemic) radial velocity in km s^{-1}. The primary radial velocity as a function of time t, $\mathrm{RV}_1(t)$, is

$$\mathrm{RV}_1(t) = K_1\,[e\cos\omega + \cos(T(t) + \omega)] + V_{\rm COM} \tag{8}$$

where

$$K_1 = \frac{2\pi a \sin i}{P\sqrt{1-e^2}}\,\frac{q}{1+q} \tag{9}$$

and the true anomaly $T(t)$ is related to the eccentric anomaly $E(t)$ by

$$\tan\frac{T(t)}{2} = \sqrt{\frac{1+e}{1-e}}\,\tan\frac{E(t)}{2} \tag{10}$$

which is iteratively solved using *Kepler*'s Equation:

$$M(t) - M_0 = 2\pi\frac{t-\tau_0}{P} = E(t) - e\sin E(t). \tag{11}$$

These parameters can be used to compute the total system mass ($M_{\rm tot} = a^3/P^2$ in solar masses) and component masses ($M_1 = M_{\rm tot}/[1+q]$, $M_2 = qM_1$).

We selected an initial parameter set that visually coincided with the primary radial velocity curve through manual experimentation, and enforced the conditions $0.2\ \mathrm{year} \leqslant P \leqslant 30\ \mathrm{year}$, $e \leqslant 0.95$, $0.005 \leqslant q \leqslant 1$, and (initially) $M_{\rm tot} \leqslant 0.3\,M_\odot$, where the last condition assumes neither primary nor secondary can be more massive than $0.15\,M_\odot$. We then computed a trial MCMC chain of 7×10^5 steps, again using the Metropolis–Hastings algorithm, with new parameters drawn from normal distributions with fixed widths $\boldsymbol{\beta} = (0.5\ \mathrm{yr},\ 0.5\ \mathrm{au},\ 0.3,\ 5^\circ,\ 5^\circ,\ 5^\circ,\ 0.2,\ 2.0\ \mathrm{km\,s^{-1}})$. Observed radial velocities were compared to model values calculated at the same epoch using a χ^2 statistic:

$$\chi^2 = \sum_{j=1}^{N_{\rm RV_1}} \frac{(\mathrm{RV}_1^{\rm (obs)}(t_j) - \mathrm{RV}_1^{\rm (model)}(t_j))^2}{\sigma^2_{\mathrm{RV}_1}(t_j)} \tag{12}$$

[9] $\bar{\theta}_{ij}$ is the average of parameter θ_j for chain i; $\bar{\theta}_j$ is the average of parameter θ_j across all chains.
[10] Modified Julian Date = Julian Date—2400000.5.

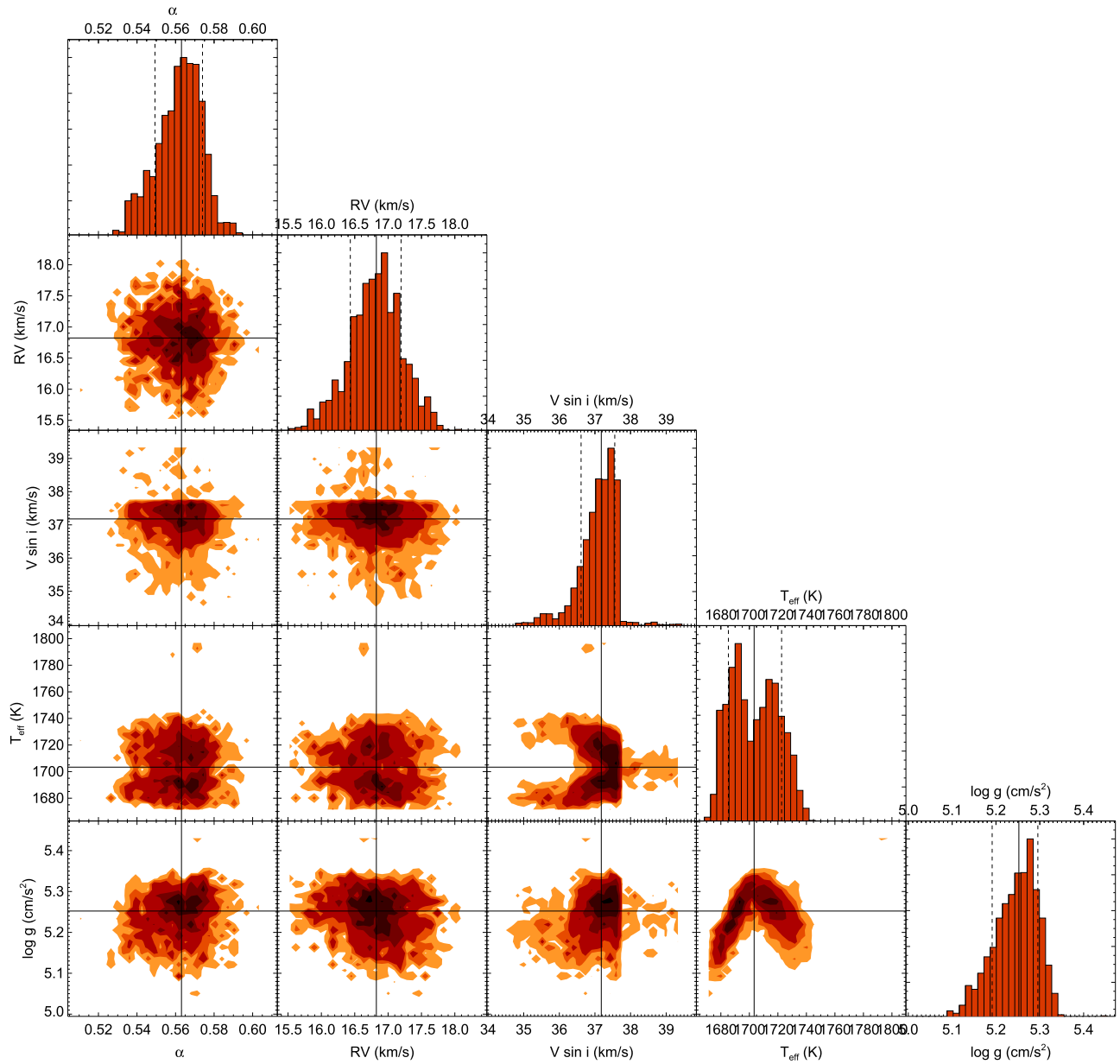

Figure 11. Parameter distributions and correlations for fit parameters RV, $V_{\rm rot}\sin i$, $T_{\rm eff}$ and $\log g$ for data taken on 2016 February 16 (UT). Contour plots show two-dimensional frequency distributions for parameter pairs, highlighting correlations. Normalized histograms at the ends of rows are marginalized over all other parameters. Median values are indicated by solid lines in all panels; 16% and 84% quantiles are indicated by dashed lines in the histograms.

where $N_{\rm RV_l} = 13$ is the number of primary RV measurements, and $\sigma_{\rm RV_l}$ the measurement errors, each with an additional 0.5 km s^{-1} systematic error added in quadrature. For a seven-parameter model, this fit had 6 degrees of freedom.

Following this initial chain, we performed $N_C = 20$ independent MCMC chains, each encompassing 10^6 steps, where the initial parameter set of each chain was chosen from uniform distributions centered on the best-fit model of the initial chain and with half-widths equal to the greater of the trial widths listed above or the standard deviations of the last 75% of the trial chain (the latter were used for i, ω, and M_0). These chains were propagated, convergence was verified for all parameters using the Gelman & Rubin (1992) scale reduction factor, and the last 75% of all chains were retained for our final distribution.

As described in the main text, two separate MCMC analyses were performed; one using a weak constraint on the total system mass ($M_{\rm tot} \leqslant 0.30\,M_\odot$), and a second using constraints based on the spectral composition of the system and the evolutionary models of Baraffe et al. (2003). The evolutionary models impose two related constraints on the orbit: first, a limit on the total system mass of $0.01\,M_\odot \leqslant M_{\rm tot} \leqslant 0.14\,M_\odot$, based on the range of system masses over 0.2–10 Gyr (Figure 3); and second, a limit on the mass function of the system:

$$f_M^{\rm (orb)} \sin i = K_{\rm l}\left(\frac{P}{2\pi G}\right)^{1/3}\sqrt{1-e^2} \leqslant a\frac{q}{1+q}\left(\frac{4\pi^2}{GP^2}\right)^{1/3}. \quad (13)$$

Assuming that $f_M^{\rm (orb)}$ cannot exceed $f_M^{\rm (evol)}$ (Equation (1)) for the oldest age modeled, we retain only solutions with $f_M^{\rm (orb)} \leqslant f_M^{\rm (evol)}(10\,{\rm Gyr}) = 0.25\,M_\odot^{1/3}$. This effectively eliminates the $P = 3$–5 years minor solutions in the unconstrained fits. The

Table 3
Fit Parameters for All NIRSPEC Observations

UT Date	Wavelength Solution			$\Delta v_{\rm inst}$ (km s^{-1})	α	RV (km s^{-1})	$V_{\rm rot}\sin i$ (km s^{-1})	$T_{\rm eff}$ (K)	$\log g$ (cgs)
	c_0 (pix)	c_1 (pix μm^{-1})	c_2 (pix μm^{-2})						
2012 Apr 02	977.55	33528.4	104426	18.1	0.565	14.3	37.7	1712	4.9
	977.52 ± 0.05	…	…	…	0.558 ± 0.012	14.7 ± 0.3	38.0 ± 0.4	2027 ± 156	5.28 ± 0.17
2012 Nov 27	971.57	33448.6	103661	20.0	0.613	7.5	37.5	1690	5.3
	971.59 ± 0.06	…	…	…	0.614 ± 0.014	7.4 ± 0.5	37.2 ± 0.7	1722 ± 32	5.35 ± 0.05
2013 Jan 20	959.50	33399.4	103745	20.3	0.523	9.1	36.6	1698	5.1
	959.48 ± 0.08	…	…	…	0.523 ± 0.012	9.1 ± 0.5	36.1 ± 0.8	1699 ± 9	5.09 ± 0.04
2013 Feb 05	959.65	33414.9	103817	20.1	0.626	7.6	37.3	1902	4.6
	959.66 ± 0.06	…	…	…	0.625 ± 0.014	7.6 ± 0.4	37.0 ± 1.2	1920 ± 50	4.67 ± 0.09
2013 Sep 17	962.59	33413.4	103221	20.8	0.802	8.0	37.1	2026	5.3
	962.59 ± 0.08	…	…	…	0.80 ± 0.02	7.8 ± 0.7	37.3 ± 1.8	2019 ± 169	5.27 ± 0.20
2013 Oct 16	962.39	33405.0	103065	18.9	0.628	10.6	37.6	1689	5.1
	962.41 ± 0.04	…	…	…	0.626 ± 0.010	10.5 ± 0.3	37.2 ± 0.5	1714 ± 172	5.12 ± 0.17
2014 Apr 13	961.84	33425.0	103765	17.5	0.550	14.2	36.7	1799	5.5
	961.84 ± 0.03	…	…	…	0.552 ± 0.010	14.4 ± 0.4	35.9 ± 0.9	2016 ± 108	5.490 ± 0.013
2014 Dec 08	957.53	33343.8	102179	18.9	0.778	6.7	26.2	1715	5.3
	957.56 ± 0.07	…	…	…	0.78 ± 0.02	6.6 ± 0.5	26.7 ± 0.9	1711 ± 17	5.27 ± 0.05
2015 Jan 01	963.11	29015.8	−41295	20.0	0.585	9.3	28.4	1727	5.1
	963.05 ± 0.09	…	…	…	0.59 ± 0.03	9.7 ± 0.8	28.4 ± 1.7	1717 ± 26	5.10 ± 0.16
2015 Dec 29	955.53	33406.1	104010	19.7	0.563	17.5	39.1	1700	5.2
	955.54 ± 0.05	…	…	…	0.560 ± 0.011	17.5 ± 0.4	39.0 ± 0.7	2031 ± 164	5.48 ± 0.13
2016 Jan 18	953.59	33347.4	102526	20.5	0.583	17.7	36.3	1700	5.3
	953.63 ± 0.06	…	…	…	0.587 ± 0.017	17.4 ± 0.4	36.1 ± 0.9	1707 ± 42	5.26 ± 0.11
2016 Feb 03	956.44	33354.6	102749	20.2	0.578	17.7	36.1	1694	5.2
	956.48 ± 0.08	…	…	…	0.57 ± 0.02	17.7 ± 0.5	35.4 ± 1.0	1708 ± 18	5.24 ± 0.05
2016 Feb 16	957.08	33390.0	102634	19.1	0.566	16.9	37.5	1691	5.2
	957.08 ± 0.05	…	…	…	0.563 ± 0.012	16.8 ± 0.4	37.2 ± 0.5	1703 ± 19	5.25 ± 0.05
2016 Apr 22	959.54	33405.9	103519	19.1	0.658	14.6	39.7	1702	5.2
	959.52 ± 0.04	…	…	…	0.656 ± 0.012	14.7 ± 0.5	39.0 ± 0.8	1802 ± 161	5.46 ± 0.14

Note. These are the fit parameters emerging from the final multi-threaded MCMC fits for each observed spectrum, excluding the coefficients for the continuum correction which were determined dynamically. The first row for each date lists the best-fit (lowest χ^2) parameters; the second row lists the means and standard deviations across all retained parameters in the MCMC chains. The coefficients for the wavelength-to-pixel conversion are defined as $p(\lambda) = \sum_{i=0}^{2} c_i(\lambda - \lambda_0)^i$, where $\lambda_0 = 2.32428$ μm. These coefficients, and the instrumental broadening, were not varied in the final MCMC fit. None of the uncertainties listed for the mean values include systematic errors, which are estimated as 0.5 km s^{-1} for RV and $V_{\rm rot}\sin i$, 50 K for $T_{\rm eff}$, and 0.25 dex for $\log g$.

mass function also provides soft constraints on the orbital inclination and age of the system. Applying the same constraint above as $f_M^{\rm (evol)}(10\,{\rm Gyr})\ \sin i \geqslant f_M^{\rm (orb)}\sin i$ to the left side of Equation (13) imposes a minimum value for $\sin i$ for a given set of orbital parameters. Conversely, requiring that $f_M^{\rm (orb)}$ be at least as large as $f_M^{\rm (evol)}$, even for $\sin i = 1$, imposes a minimum constraint on the component masses and hence minimum model age of the system. The distributions of these minimum parameters for all the orbital fits are shown in Figure 8.

To examine predictions for projected separation and primary astrometric perturbation, we combined our seven-parameter model set with the trignometric distance of SDSS J0805 +4812, $d = 23.2 \pm 0.5$ pc (Dupuy & Liu 2012) to calculate the projected angular separation vector from primary component to secondary component, $\boldsymbol{\rho} = (\Delta\alpha(t), \Delta\delta(t))$. This was determined from

$$\Delta\alpha(t) = \frac{a}{d}[A(\cos E(t) - e) + F\sqrt{1-e^2}\sin E(t)] \quad (14)$$

$$\Delta\delta(t) = \frac{a}{d}[B(\cos E(t) - e) + G\sqrt{1-e^2}\sin E(t)] \quad (15)$$

where $\Delta\alpha$ and $\Delta\delta$ are the angular separations on the sky measured in arcseconds, and A, B, F and G are the Thiele-Innes constants (Innes 1907; van den Bos 1927):

$$A = \cos\omega\cos\Omega - \sin\omega\sin\Omega\cos i \quad (16)$$

$$B = \cos\omega\sin\Omega + \sin\omega\cos\Omega\cos i \quad (17)$$

$$F = -\sin\omega\cos\Omega - \cos\omega\sin\Omega\cos i \quad (18)$$

$$G = -\sin\omega\sin\Omega + \cos\omega\cos\Omega\cos i. \quad (19)$$

Here, Ω is the longitude of ascending node, for which we had no constraints, so a uniform distribution of $0 \leqslant \Omega \leqslant 360^\circ$ was assumed. The amplitude of astrometric variability was computed from projected angular separation

$$\rho_{\rm ast} = \rho(f_F - f_M) \quad (20)$$

where

$$f_F = \frac{f_1}{f_1 + f_2} = (1 + 10^{0.4\Delta m})^{-1} \quad (21)$$

$$f_M = \frac{M_2}{M_1 + M_2} \quad (22)$$

is the fractional primary flux, with $\Delta m = m_2 - m_1$; and the fractional secondary mass, respectively. To compare to the MKO J-band measurements of Dupuy & Liu (2012), we assumed $\Delta m = 1.8$ based on the spectral template fitting in Section 3.

REFERENCES

Allard, F., Homeier, D., & Freytag, B. 2011, in ASP Conf. Ser. 448, 16th Cambridge Workshop on Cool Stars, Stellar Systems, and the Sun, ed. C. Johns-Krull, M. K. Browning, & A. A. West (San Francisco, CA: ASP), 91
Allard, F., Homeier, D., & Freytag, B. 2012, RSPTA, 370, 2765
Allen, P. R. 2007, ApJ, 668, 492
Baraffe, I., Chabrier, G., Barman, T. S., Allard, F., & Hauschildt, P. H. 2003, A&A, 402, 701
Bardalez Gagliuffi, D. C., Burgasser, A. J., Gelino, C. R., et al. 2014, ApJ, 794, 143
Bardalez Gagliuffi, D. C., Gelino, C. R., & Burgasser, A. J. 2015, AJ, 150, 163
Basri, G., & Martín, E. L. 1999, AJ, 118, 2460
Bate, M. R. 2009, MNRAS, 392, 590
Bate, M. R. 2012, MNRAS, 419, 3115
Bildsten, L., Brown, E. F., Matzner, C. D., & Ushomirsky, G. 1997, ApJ, 482, 442
Blake, C. H., Charbonneau, D., White, R. J., et al. 2008, ApJL, 678, L125
Blake, C. H., Charbonneau, D., & White, R. J. 2010, ApJ, 723, 684
Borkovits, T., Derekas, A., Kiss, L. L., et al. 2013, MNRAS, 428, 1656
Bouy, H., Brandner, W., Martín, E. L., et al. 2003, AJ, 126, 1526
Bouy, H., Duchêne, G., Köhler, R., et al. 2004, A&A, 423, 341
Burgasser, A. J. 2007, AJ, 134, 1330
Burgasser, A. J. 2014, ASInC, 11, 7
Burgasser, A. J., & Blake, C. H. 2009, AJ, 137, 4621
Burgasser, A. J., Cruz, K. L., Cushing, M., et al. 2010, ApJ, 710, 1142
Burgasser, A. J., Gillon, M., Melis, C., et al. 2015, AJ, 149, 104
Burgasser, A. J., Liu, M. C., Ireland, M. J., Cruz, K. L., & Dupuy, T. J. 2008, ApJ, 681, 579
Burgasser, A. J., Luk, C., Dhital, S., et al. 2012, ApJ, 757, 110
Burgasser, A. J., Reid, I. N., Siegler, N., et al. 2007, in Protostars and Planets V, ed. B. Reipurth, D. Jewitt, & K. Keil (Tucson, AZ: Univ. Arizona Press), 427
Burrows, A., Heng, K., & Nampaisarn, T. 2011, ApJ, 736, 47
Cruz, K. L., Burgasser, A. J., Reid, I. N., & Liebert, J. 2004, ApJL, 604, L61
Dahn, C. C., Harris, H. C., Levine, S. E., et al. 2008, ApJ, 686, 548
Deleuil, M., Deeg, H. J., Alonso, R., et al. 2008, A&A, 491, 889
Duchêne, G., & Kraus, A. 2013, ARA&A, 51, 269
Dupuy, T. J., Allen, P. R., Kraus, A. L., et al. 2013, AN, 334, 36
Dupuy, T. J., & Liu, M. C. 2011, ApJ, 733, 122
Dupuy, T. J., & Liu, M. C. 2012, ApJS, 201, 19
Dupuy, T. J., Liu, M. C., & Ireland, M. J. 2009, ApJ, 692, 729
Dupuy, T. J., Liu, M. C., & Ireland, M. J. 2014, ApJ, 790, 133
Filippazzo, J. C., Rice, E. L., Faherty, J., et al. 2015, ApJ, 810, 158
Gelman, A., & Rubin, D. B. 1992, StaSc, 7, 457
Golimowski, D. A., Leggett, S. K., Marley, M. S., et al. 2004, AJ, 127, 3516
Goodman, J., & Weare, J. 2010, Commun. Appl. Math. Comput. Sci., 5, 65
Harding, L. K., Hallinan, G., Konopacky, Q. M., et al. 2013, A&A, 554, A113
Hastings, W. K. 1970, Biometrika, 57, 97
Hawley, S. L., Covey, K. R., Knapp, G. R., et al. 2002, AJ, 123, 3409
Hayashi, C., & Nakano, T. 1963, PThPh, 30, 460
Innes, R. T. A. 1907, Obs, 30, 310
Joergens, V., Müller, A., & Reffert, S. 2010, A&A, 521, A24
Johnson, J. A., Apps, K., Gazak, J. Z., et al. 2011, ApJ, 730, 79
Kasper, M., Burrows, A., & Brandner, W. 2009, ApJ, 695, 788
Khandrika, H., Burgasser, A. J., Melis, C., et al. 2013, AJ, 145, 71
Knapp, G. R., Leggett, S. K., Fan, X., et al. 2004, AJ, 127, 3553
Konopacky, Q. M., Ghez, A. M., Barman, T. S., et al. 2010, ApJ, 711, 1087
Kramida, A., Ralchenko, Yu., Reader, J. & NIST ASD Team 2014, NIST Atomic Spectra Database (version 5.2), (Gaithersburg, MD: NIST), http://http://physics.nist.gov/asd
Kratter, K. M. 2011, in ASP Conf. Ser. 447, Evolution of Compact Binaries, ed. L. Schmidtobreick, M. R. Schreiber, & C. Tappert (San Francisco, CA: ASP), 47
Kraus, A. L., Ireland, M. J., Martinache, F., & Lloyd, J. P. 2008, ApJ, 679, 762
Kumar, S. S. 1962, AJ, 67, 579
Kumar, S. S. 1963, ApJ, 137, 1121
Liu, M. C., Dupuy, T. J., & Leggett, S. K. 2010, ApJ, 722, 311
Liu, M. C., & Leggett, S. K. 2005, ApJ, 634, 616
Livingston, W., & Wallace, L. 1991, An Atlas of the Solar Spectrum in the Infrared from 1850 to 9000 cm^{-1} (1.1 to 5.4 micrometer), NSO Technical Rep. (Tucson, AZ: National Solar Observatory)
Looper, D. L., Gelino, C. R., Burgasser, A. J., & Kirkpatrick, J. D. 2008, ApJ, 685, 1183
Magazzu, A., Martin, E. L., & Rebolo, R. 1991, A&A, 249, 149
Marocco, F., Andrei, A. H., Smart, R. L., et al. 2013, AJ, 146, 161
Martin, E. L., Rebolo, R., & Magazzu, A. 1994, ApJ, 436, 262
Mazeh, T., & Zucker, S. 1994, Ap&SS, 212, 349
McLean, I. S., Graham, J. R., Becklin, E. E., et al. 2000, Proc. SPIE, 4008, 1048
Metropolis, N., Rosenbluth, A. W., Rosenbluth, M. N., Teller, A. H., & Teller, E. 1953, JChPh, 21, 1087
Offner, S. S. R., Kratter, K. M., Matzner, C. D., Krumholz, M. R., & Klein, R. I. 2010, ApJ, 725, 1485
Parker, R. J., & Meyer, M. R. 2014, MNRAS, 442, 3722
Radigan, J., Jayawardhana, R., Lafrenière, D., et al. 2012, ApJ, 750, 105
Reid, I. N., Gizis, J. E., Kirkpatrick, J. D., & Koerner, D. W. 2001, AJ, 121, 489
Reid, I. N., Kirkpatrick, J. D., Gizis, J. E., et al. 2000, AJ, 119, 369
Reid, I. N., Kirkpatrick, J. D., Liebert, J., et al. 2002, AJ, 124, 519
Sahlmann, J., Lazorenko, P. F., Ségransan, D., et al. 2013, A&A, 556, A133
Schaffenroth, V., Geier, S., Heber, U., et al. 2014, A&A, 564, A98
Stassun, K. G., Mathieu, R. D., & Valenti, J. A. 2006, Natur, 440, 311
Stephens, D. C., Leggett, S. K., Cushing, M. C., et al. 2009, ApJ, 702, 154
Torres, G., Andersen, J., & Giménez, A. 2010, A&ARv, 18, 67
Tuthill, P., Lloyd, J., Ireland, M., et al. 2006, Proc. SPIE, 6272, 62723A
Ushomirsky, G., Matzner, C. D., Brown, E. F., et al. 1998, ApJ, 497, 253
van Dam, M. A., Bouchez, A. H., Le Mignant, D., et al. 2006, PASP, 118, 310
van den Bos, W. H. 1927, BAN, 3, 261
Wizinowich, P. L., Le Mignant, D., Bouchez, A. H., et al. 2006, PASP, 118, 297
York, D. G., Adelman, J., Anderson, J. E., Jr., et al. 2000, AJ, 120, 1579